Opto-Electronic Advances

ISSN 2096-4579 CN 51-1781/TN

Polariton lasing in Mie-resonant perovskite nanocavity

Mikhail A. Masharin, Daria Khmelevskaia, Valeriy I. Kondratiev, Daria I. Markina, Anton D. Utyushev, Dmitriy M. Dolgintsev, Alexey D. Dmitriev, Vanik A. Shahnazaryan, Anatoly P. Pushkarev, Furkan Isik, Ivan V. Iorsh, Ivan A. Shelykh, Hilmi V. Demir, Anton K. Samusev and Sergey V. Makarov

Citation: Masharin MA, Khmelevskaia D, Kondratiev VI, et al. Polariton lasing in Mie-resonant perovskite nanocavity. *Opto-Electron Adv* **7**, 230148(2024).

https://doi.org/10.29026/oea.2024.230148

Received: 19 August 2023; Accepted: 19 January 2024; Published online: 25 April 2024

Opto-Electronic Advances

Article

April 2024, Vol. 7, No. 4

DOI: 10.29026/oea.2024.230148

Polariton lasing in Mie-resonant perovskite nanocavity

Mikhail A. Masharin[1,2†], Daria Khmelevskaia[2†], Valeriy I. Kondratiev[2], Daria I. Markina[2], Anton D. Utyushev[2], Dmitriy M. Dolgintsev[2], Alexey D. Dmitriev[2], Vanik A. Shahnazaryan[2,3], Anatoly P. Pushkarev[2], Furkan Isik[1,4], Ivan V. Iorsh[2,5], Ivan A. Shelykh[3,6], Hilmi V. Demir[1,4*], Anton K. Samusev[2,7*] and Sergey V. Makarov[2,8*]

Deeply subwavelength lasers (or nanolasers) are highly demanded for compact on-chip bioimaging and sensing at the nanoscale. One of the main obstacles for the development of single-particle nanolasers with all three dimensions shorter than the emitting wavelength in the visible range is the high lasing thresholds and the resulting overheating. Here we exploit exciton-polariton condensation and mirror-image Mie modes in a cuboid $CsPbBr_3$ nanoparticle to achieve coherent emission at the visible wavelength of around 0.53 μm from its ultra-small (≈0.007 μm^3 or ≈λ^3/20) semiconductor nanocavity. The polaritonic nature of the emission from the nanocavity localized in all three dimensions is proven by direct comparison with corresponding one-dimensional and two-dimensional waveguiding systems with similar material parameters. Such a deeply subwavelength nanolaser is enabled not only by the high values for exciton binding energy (≈35 meV), refractive index (>2.5 at low temperature), and luminescence quantum yield of $CsPbBr_3$, but also by the optimization of polaritons condensation on the Mie resonances with quality factors improved by the metallic substrate. Moreover, the key parameters for optimal lasing conditions are intermode free spectral range and phonons spectrum in $CsPbBr_3$, which govern polaritons condensation path. Such chemically synthesized colloidal $CsPbBr_3$ nanolasers can be potentially deposited on arbitrary surfaces, which makes them a versatile tool for integration with various on-chip systems.

Keywords: nanolaser; perovskite; polariton; Mie resonance; exciton-polariton

Masharin MA, Khmelevskaia D, Kondratiev VI et al. Polariton lasing in Mie-resonant perovskite nanocavity. *Opto-Electron Adv* **7**, 230148 (2024).

[1]UNAM-Institute of Materials Science and Nanotechnology, National Nanotechnology Research Center, Department of Electrical and Electronics Engineering, Department of Physics, Bilkent University, Ankara 06800, Turkey; [2]ITMO University, School of Physics and Engineering, St. Petersburg 197101, Russia; [3]Abrikosov Center for Theoretical Physics, MIPT, Dolgoprudnyi, Moscow Region 141701, Russia; [4]LUMINOUS! Center of Excellence for Semiconductor Lighting and Displays, School of Electrical and Electronic Engineering, School of Physical and Mathematical Sciences, School of Materials Science and Engineering, Nanyang Technological University, Singapore 639798, Singapore; [5]Department of Physics, Engineering Physics and Astronomy, Queen's University, Kingston, Ontario K7L 3N6, Canada; [6]Science Institute, University of Iceland, Dunhagi 3, IS-107, Reykjavik, Iceland; [7]Experimentelle Physik 2, Technische Universität Dortmund, Dortmund 44227, Germany; [8]Qingdao Innovation and Development Center, Harbin Engineering University, Qingdao 266000, China.

[†]These authors contributed equally to this work.

*Correspondence: HV Demir,E-mail: volkan@fen.bilkent.edu.tr; AK Samusev, E-mail: a.samusev@metalab.ifmo.ru; SV Makarov, E-mail: s.makarov@metalab.ifmo.ru

Received: 19 August 2023; Accepted: 19 January 2024; Published online: 25 April 2024

Introduction

Nowadays, compact lasers are gradually replacing and complementing electrical interconnects, with billions of devices deployed since 1990s[1]. In turn, the increase of optical elements on a photonic chip is another technological trend requiring integrated lasers with the smallest possible volume[2,3]. Thus, continuing laser source miniaturization is a natural approach to lowering energy consumption and creating compact devices with various functionalities[4–6]. Pioneering works on near- and subwavelength lasers date back to the turn of the century with the demonstration of whispering-gallery semiconductor microdisk lasers[7], InGaAsP based photonic crystal lasers[8] and ZnO nanowire lasers[9]. Further progress is directed towards the use of new gain materials and advanced design configurations: metal-based resonant-cavity structures[10,11], nanoantenna arrays[12] and bound-state-in-continuum systems[13–17]. In these and many other designs[10–18], optical modes are confined in one or two dimensions, where one of the sizes remains larger than the mode wavelength. The nanolasers where all geometrical parameters are truly subwavelength were demonstrated in a very limited number of works due to high technological requirements to materials and cavity design[19–21]. Indeed, these limitations prevent the creation of all-subwavelength nanolasers for visible range, except colloidal nanolasers where observation of lasing from a single nanolaser is still a challenge. When the size of photonic nanocavity becomes comparable to the wavelength in material, the Q-factor of optical modes drastically decreases, requiring higher thresholds and even becoming shape-independent[22]. In turn, a polariton laser does not require inversion of population and, thus, can work at much lower charge carrier densities as compared with classical lasers[23]. These inversion-free lasers were theoretically predicted in 1996[24], whereas the first demonstration of lasers and Bose–Einstein condensate (BEC) dates back to the early 2000s[25,26]. As half-matter half-light systems, polariton lasers promised ultra-low threshold carrier densities, around two orders of magnitude lower compared with conversion photonic lasers[26], opening up a new avenue for further laser compactization.

One of the most suitable light-emitting materials for supporting a polariton lasing is cesium lead bromide $CsPbBr_3$ perovskite owing to high photoluminescence (PL) quantum yield up to 95%[27], defect tolerance[28], strong excitons[29,30] with a high refractive index around the excitonic state[31], high gain[32], and ultrafast optical response[33]. Polariton condensation and lasing in various $CsPbBr_3$ cavities was shown in $CsPbBr_3$ nanowires[34], microplates[35], and more complex systems[36–40]. Remarkably, phonons in $CsPbBr_3$ containing heavy ions possess energies just up to 38 meV,[41] which can play a crucial role in the polaritons condensation in the case of small cavities with large inter-mode spectral separation, paving the way to the efficient operation of nanolasers.

In this work, we exploit an inversion-free regime for a polariton nanolaser with a record small volume $(\lambda/2.7)^3$ among all known perovskite lasers. Here the polariton nature of lasing is proved experimentally based on the direct comparison of 2D, 1D, and 0D perovskite waveguiding and resonant systems, as well as by analytical modeling. The detailed experimental study and numerical full-wave calculations allow us to find a cavity design made of $CsPbBr_3$ with the smallest volume supporting lasing at low temperatures. Namely, a mirror-image quadrupole Mie mode in a nanocuboidal $CsPbBr_3$ particle on silver film allows for a high-enough quality factor (Q) and inter-mode spectral distance, which is larger than the highest energy of optical phonon in $CsPbBr_3$. From a technological point of view, the developed method for colloidal synthesis of the lasing nanoparticles (NPs) enables the simple deposition of nanolasers, which makes it suitable for on-chip integration with various photonic circuits.

Results

Concept of polariton stimulated relaxation in different perovskite structures

First, let us discuss the concept of polariton stimulation in a nonlinear regime in perovskite thin films, nanowires, and nanocubes (Fig. 1(a)) upon a non-resonant (i.e. excited by photons with the energy higher than that for the exciton state) optical pump. Each of these perovskite structures supports exciton-polariton states, schematically shown in Fig. 1(b), where a guided polariton in the film has a dispersion curve below the light cone[42]; in a nanowire, the waveguided mode has quantized F-P resonances[43]; and polaritons in a Mie-resonant cavity do not have angular dispersion, but red-shifted from their uncoupled states[44]. Exciton-polaritons in these structures can be excited non-resonantly by a femtosecond (fs) laser pulse, as we show experimentally in the next sections. Varying the pump fluence one can control the number of polaritons in the system. At the low pump

fluences around F_1, the photoexcited carriers thermalize forming excitons and exciton-polaritons in the available states (red and green dots, respectively, in Fig. 1(b)). The formed polaritons relax to lower energies through phonon scattering and then recombine[23]. Nonlinear properties start to play a significant role at the higher pump fluences F_2 when stimulated relaxation and hence stimulated emission appear. Large exciton and polariton concentrations cause nonlinear boson stimulation[45], which leads to the polariton accumulation at some specific state on the polariton branch, where polaritons still have high exciton fraction, but low non-radiative losses (Fig. 1(c)). The recombination of the accumulated polaritons, which occupy one quantum state, provides the coherence of the emission. At this moment one can mention there are no observable differences between the stimulated polariton emission and the well-known amplified spontaneous emission (ASE) except for the origin of the coherence[23]. However, for even higher pump fluences F_3, polaritons start interacting at the accumulated levels, leading to

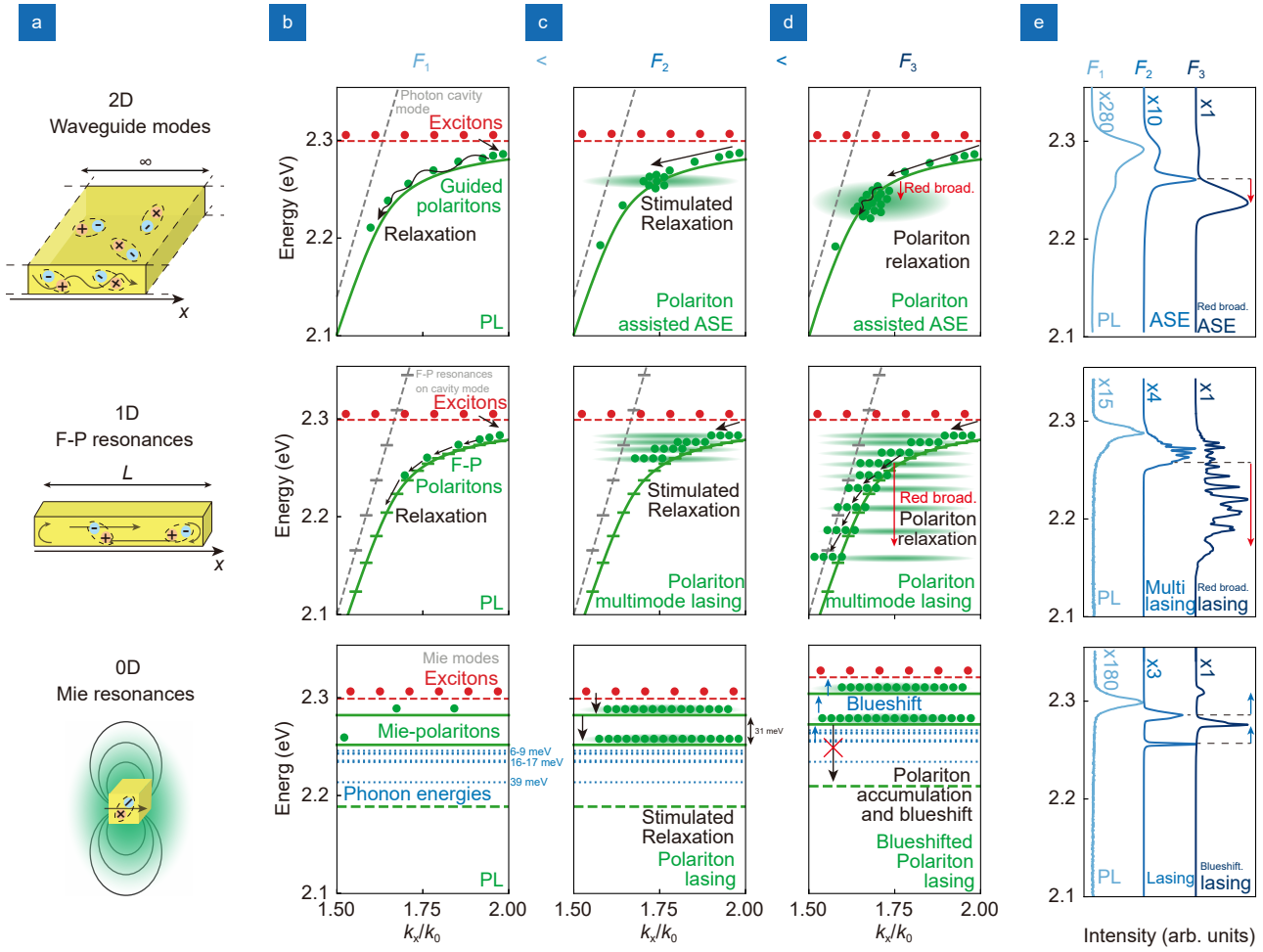

Fig. 1 | The concept of the stimulated polariton emission in low-dimensional perovskite photon cavities. (**a**) Illustration of studied perovskite structures: thin film (2D), nanowire (1D) and nanocube (0D). (**b**) Scheme of the linear PL regime, estimated photon cavity modes (grey dashed lines) strongly coupled with exciton resonance (red dashed lines) resulting in exciton-polariton formation (green lines) for each of the structures. Green dashed lines show unobserved, but theoretically predicted polariton state. Dashed blue lines in the lower plot show the existing phonon energies, counted from the second Mie-polariton state. Uncoupled Mie-polariton states are beyond the given energy range. Waveguide mode in 2D perovskite film results in a guided polariton; Quantized Fabry-Perot (F-P) states originating from waveguide mode in 1D nanowires resulting in F-P polariton resonances; Mie resonances supported in 0D nanocubes results in Mie-polaritons. Red circles represent excitons in the systems, and green circles correspond to exciton-polaritons. (**c**) Scheme of the stimulated polariton relaxation appeared in the different systems with increasing the pump fluence $F_2 > F_1$ which leads to the onset of ASE in 2D thin films, multimode lasing in 1D nanowire structure, and few-mode lasing in 0D nanocubes. (**d**) Scheme of the polariton interaction at higher pump fluences $F_3 > F_2$. Polaritons in 2D and 1D relax at lower energy, and in 0D they accumulate at the ground level, which blueshifts with increase of pump fluence. (**e**) Measured normalized emission spectra at pump fluences F_1, F_2, F_3 from each of the perovskite structures. The colors of the spectra correspond to the fluences of F_1, F_2, F_3 respectively in (b–d).

different phenomena. If polariton states at lower energies exist, like for guided polaritons or F-P polaritons, the polaritons scatter to the lower energy states[46]. In the case of perovskite nanocubes, where there can be no states or the difference between the neighboring levels is larger than existing phonon energies, polaritons are not able to thermalize. Therefore, they stronger accumulate in larger numbers at the available states, which leads to the polariton-polariton Coulomb interaction and polariton blueshift, observed in polariton systems (Fig. 1(d))[36,37].

The discussion of the concept can be supported by the bosonic kinetic model, limiting to the three discrete polariton levels for simplicity. We attribute each of the levels to a quantized excitonic eigenmode. The non-resonant pulsed excitation creates a large non-equilibrium population of electrons and holes, forming the exciton reservoir with the number of excitons n_{R}, which plays as a feeding source for the three bright exciton levels with energies $E_{X1} < E_{X2} < E_{X3}$. We also consider the transitions between different excitonic levels. As the energy gaps between the peaks are of the order of tens of meV, we assume that optical phonons mediate these transitions[47,48]. In all the transitions, we take into account the bosonic nature of excitons, resulting in $\propto n_i(n_j+1)$ type terms. The system of equations describing the dynamics can be derived within the standard approach for polaritonic mode occupation[49–51] and have a form:

$$\begin{aligned}
\frac{\mathrm{d}n_{\mathrm{R}}}{\mathrm{d}t} =& P(t) - \left[\gamma_{\mathrm{R}} + \alpha_3(n_3+1) + \alpha_2(n_2+1) \right.\\
&\left. + \alpha_1(n_1+1)\right] n_{\mathrm{R}} \ ,\\
\frac{\mathrm{d}n_3}{\mathrm{d}t} =& \alpha_3 n_{\mathrm{R}}(n_3+1) - \left(\frac{1}{\tau_3^{\mathrm{r}}} + \frac{1}{\tau_3^{\mathrm{nr}}} + \gamma^{(2)} n_3\right) n_3\\
&+ \frac{1}{\tau_{32}}\left[\mathrm{e}^{-\beta\Delta_{32}} n_2(n_3+1) - n_3(n_2+1)\right]\\
&+ \frac{1}{\tau_{31}}\left[\mathrm{e}^{-\beta\Delta_{31}} n_1(n_3+1) - n_3(n_1+1)\right] \ ,\\
\frac{\mathrm{d}n_2}{\mathrm{d}t} =& \alpha_2 n_{\mathrm{R}}(n_2+1) - \left(\frac{1}{\tau_2^{\mathrm{r}}} + \frac{1}{\tau_2^{\mathrm{nr}}} + \gamma^{(2)} n_2\right) n_2\\
&+ \frac{1}{\tau_{32}}\left[n_3(n_2+1) - \mathrm{e}^{-\beta\Delta_{32}} n_2(n_3+1)\right]\\
&+ \frac{1}{\tau_{21}}\left[\mathrm{e}^{-\beta\Delta_{21}} n_1(n_2+1) - n_2(n_1+1)\right] \ ,\\
\frac{\mathrm{d}n_1}{\mathrm{d}t} =& \alpha_1 n_{\mathrm{R}}(n_1+1) - \left(\frac{1}{\tau_1^{\mathrm{r}}} + \frac{1}{\tau_1^{\mathrm{nr}}} + \gamma^{(2)} n_1\right) n_1\\
&+ \frac{1}{\tau_{31}}\left[n_3(n_1+1) - \mathrm{e}^{-\beta\Delta_{31}} n_1(n_3+1)\right]\\
&+ \frac{1}{\tau_{21}}\left[n_2(n_1+1) - \mathrm{e}^{-\beta\Delta_{21}} n_1(n_2+1)\right] \ , \qquad (1)
\end{aligned}$$

where $P(t) = P_0 \mathrm{e}^{-(t-t_0)^2/(2\tau_{\mathrm{p}}^2)}$ stands for pulsed non-resonant pump, α_i denote the scattering rate from the reservoir to the i-th excitonic level, $\tau_i^{\mathrm{r[nr]}}$ are radiative [non-radiative] lifetimes of excitons, and $\gamma^{(2)}$ is the exciton-exciton annihilation rate. Here $\beta = 1/k_{\mathrm{B}}T$, with k_{B} being the Boltzmann constant, τ_{ij}, $\Delta_{ij} = |E_i - E_j|$ denote the transition rates and the energy gaps between different exciton levels. The respective emission is estimated as $I_i \propto \int n_i(t)\mathrm{d}t/\tau_i^{\mathrm{r}}$. The results of the simulation will be demonstrated in the next section and here we qualitatively discuss the process.

At the low amplitude of $P(t)$, only linear terms of n_{R} play a significant role as a source of the particles for all three levels, and linear terms of radiative and non-radiative lifetimes $\tau_{1-3}^{\mathrm{r,nr}}$ provide the quasiparticles annihilation. After some threshold, the nonlinear term of $n_{\mathrm{R}}n_3$ in the second equation of the system Eq. (1) causes stimulated relaxation of the quasiparticles to the n_3 level, resulting in polariton stimulated emission. At the same time, it dramatically increases the rate of the quasiparticle scattering from n_3 to n_2 with a characteristic time of τ_{32}. With further increase of the $P(t)$ and, therefore n_{R}, the terms of $1/\tau_{32}n_3n_2$ and $\alpha_2 n_{\mathrm{R}}n_2$ cause the stimulation to the lower n_2, providing the stimulated emission from the second level. Similarly, at some higher pump threshold, the stimulated relaxation reaches the n_1 via quadratic n terms in the equations. The values of the thresholds are determined by the characteristic scattering times τ and the rate of the scattering from the reservoir n_{R} to the polariton levels α, which depend on the phonon energies and the exciton fraction in the polariton. This approach of the three-level model is implemented for the 0D case of nanocuboid lasing, well corresponding to the experimental observations (dashed lines in Fig. 3(h)). Moreover, in 1D and 2D systems, the process of the stimulated polariton relaxation can be described in a similar way, but with a continuous spectrum of the polariton states.

In order to qualitatively support the above-mentioned concept of polariton lasing, we demonstrate measured emission spectra integrated over angles and obtained under non-resonant fs pump with different pump fluences for lead-bromide perovskite thin film, nanowire, and nanocuboid (Fig. 2(a, f, k), respectively) at $T = 6$ K in Fig. 1(e). At pump fluence F_1 in the linear regime, we observe linear PL spectra with tails in the red region. However, it should be noted that the asymmetric PL spectra origin is still under discussion and could originate

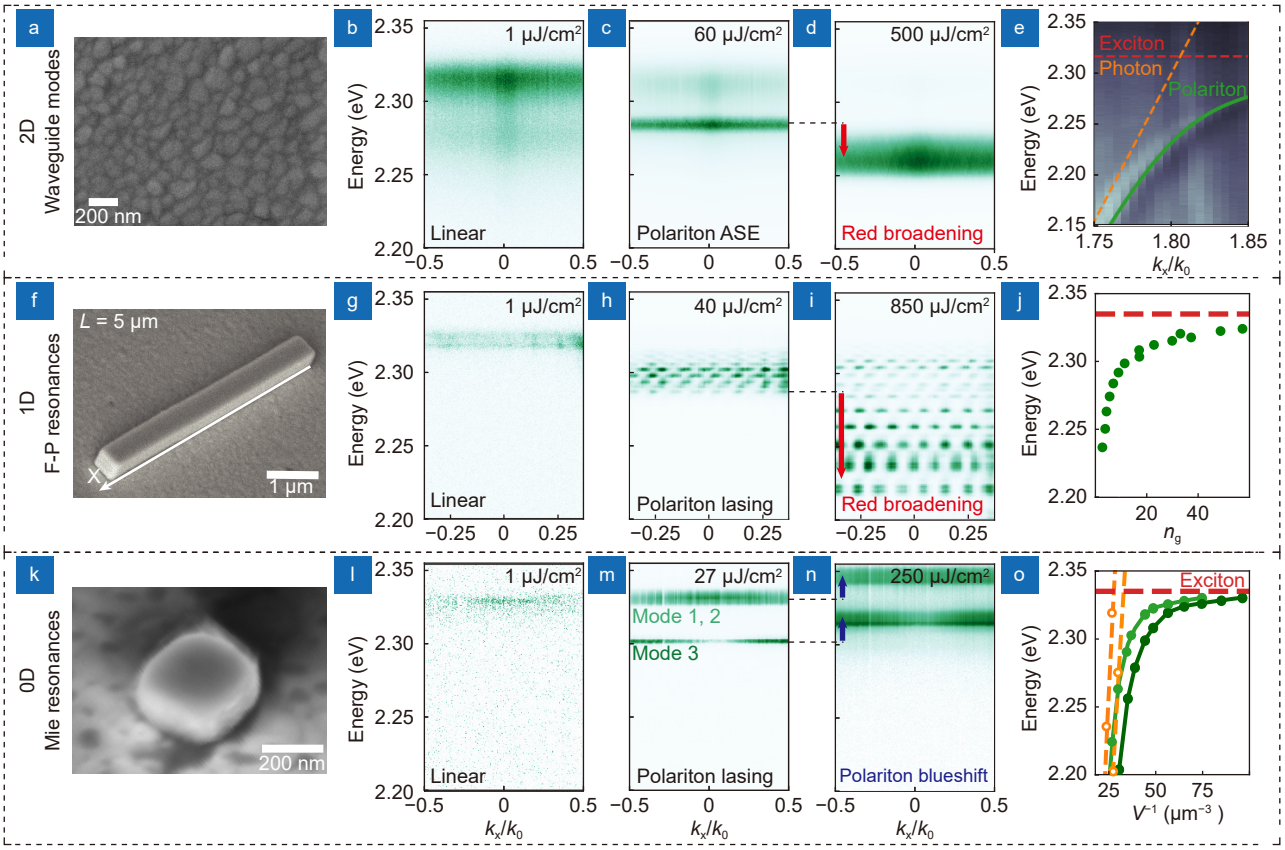

Fig. 2 | Measurements of the stimulated emission of perovskite thin film, nanowire, and nanocuboid. (**a**) SEM image of the studied perovskite thin film. (**b–d**) Angle-resolved emission spectra of the thin film, obtained under a non-resonant fs pump at 6 K for pump fluences of 1, 60, and 500 μJ/cm², which correspond to the linear PL, polariton ASE, and red-broadened polariton ASE, respectively. (**e**) Angle-resolved reflection spectra of the guided guided mode, measured at room temperature below the light cone. The dashed orange line shows the estimated uncoupled photon mode, the dashed red line shows the estimated exciton level and the solid green line shows the fitted polariton mode. (**f**) SEM image of the studied perovskite nanowhisker with a length of around 5 μm. (**g–j**) Angle-resolved emission measurements of the nanowire for pump fluences of 1, 40, and 850 μJ/cm², respectively. The data shows the dynamics of polariton multimode lasing emission. (j) The group refractive index of the studied nanowire as a function of the energy, estimated from the FSR of lasing peaks (See SI for the details). (**k**) SEM image of the studied perovskite nanocuboid. (**l–n**) Angle-resolved emission measurements of the nanocuboid for pump fluences of 1, 27, and 250 μJ/cm², respectively. (**o**) The estimated spectral position of the mode as a function of the inverted volume.

from other effects, such as defect states and PL re-absorption[48,52,53]. Increasing pump fluence up to F_2 ASE in the film, multimode lasing in the nanowire, and few-mode lasing in nanocuboid appear. According to the concept discussed above stimulated emission shifts to the red region in 2D and 1D structures and to the blue region in 0D at the highest F_3 pump fluence (Fig. 1(e)).

To experimentally check if we are below the Mott transition, we further increase the pump fluence up to 3 mJ/cm² for the nanocuboids and observe the broad PL spectrum without lasing modes with the shifted central peak from the initial exciton PL up to the 32 meV, which is very close to the value of exciton binding energy (see Fig. S4 in SI for the details). Nevertheless, even under the Mott transition, electron-hole pairs can still be correlated to Bardeen–Cooper–Schrieffer (BCS) states, which strongly couples to the optical mode, resulting in BCS polaritons[54]. This phenomenon allows observing polariton stimulation and condensation even above the Mott transition. Experimentally collected data, shown in Fig. 1(e), supports the polariton stimulation model only indirectly, and in the following sections, we show more experimental insights, supporting the idea.

According to the conventional approach, the spectral position of the optical gain profile and ASE shifts to the blue region and grows in intensity with increasing pump fluence in semiconductors[55,56]. Nevertheless, in perovskite structures, we observe controversial results (Fig. 1(e)), which can be explained by exciton-polariton relaxation discussed above. In order to check the assumption we have to get rid of exciton-polaritons in the system with lead-bromide perovskites. As the exciton state in

the material is stable at room temperature and the high refractive index provides strong field localization in a variety of bulk perovskite structures, we can turn to the colloidal perovskite nanoparticles. In this case, random fluctuations of the nanoparticles in the solution prevent strong light-matter coupling and can be considered a non-polariton system. Indeed, the measured gain profile in the system in ref.[57] represents a clear conventional gain profile blueshift with pump fluence increasing rather than red broadening.

The role of exciton-polaritons in the lead-bromide perovskite structures is important from a fundamental understanding of the process and it also reveals new efficient approaches for the nanolaser designs. In the following sections, we properly prove the presence of exciton-polaritons in the studied structures and suggest a new approach for efficient inversion-free nanolasers based on the Mie-polaritons.

Exciton-polariton stimulated emission in different perovskite structures

First, we experimentally study exciton-polaritons in 2D perovskite structures — polycrystalline thin films, which are synthesized by solvent engineering method (See *Methods* for the details). Synthesized films, shown in Fig. 2(a), have roughness equal to 5.1 nm, for 120 nm film width (See Fig. S12 in SI for more details).

We use non-resonant fs emission with a photon energy of 2.53 eV and 100 kHz of repetition rate to measure emission spectra with angular resolution (Fig. 2(b, c)). At low pump fluence around 1 μJ/cm^2 linear excitonic PL spectrum without any pronounced radiation pattern is observed (Fig. 2(b)). The low intensive broad peak in the red region can be attributed to guided polaritons scattered on morphology defects and grain boundaries. With increasing the pump fluence up to 60 μJ/cm^2 a wide ASE peak appears at the energy around 2.27 eV. The ASE emission strongly broadens toward the red region with increasing pump fluence (Fig. 2(d)), as was discussed in the previous section.

To confirm the polaritonic nature of the ASE, we directly measure waveguide mode dispersion at room temperature by the angle-resolved spectroscopy method combined with a solid immersion lens (SIL, see *Methods* for the details). The method allows for measurement of guided mode as a function of the wavenumber below the light cone through leakage tails, collected by the SIL. The angle-resolved reflection spectrum of the thin film below the light cone is shown in Fig. 2(e). In the measured spectra, one can mention pronounced curvature near exciton resonance, which is a sign of the strong light-matter coupling regime. We extract guided mode dispersion from the experimental data and fit it by the two-coupled oscillator model to evaluate a light-matter coupling regime[58] (see *Methods* for the fitting details). As a result, the estimated light-matter coupling coefficient $g_0 = 72$ meV and Rabi splitting $\Omega_{\text{Rabi}} = 143$ meV are much larger, than the photon and exciton linewidths, which are estimated to be 30 and 20 meV, respectively. Therefore, the strong coupling regime and guided polariton in the perovskite thin film are confirmed[58]. It should be mentioned that the angle-resolved spectroscopy with SIL is possible to realize only at room temperature and the strong light-matter coupling regime is confirmed at these conditions. Moreover, we also observe ASE with angular resolution below the light cone originating from the guided mode and can be controlled by the optical losses (see Section 1 of SI). However, at cryogenic temperatures, non-radiative losses are reduced and the exciton fraction in the photoinduced carriers is increasing[59]. Therefore, if exciton-polaritons exist at room temperature, they have to exist at cryogenic temperatures as well, where all our measurements are carried out[60].

In recent works, lead-bromide nanowires demonstrated high-quality lasing emission at the room-temperature under pulsed and even CW-pump optical pump[43,61]. Nevertheless, our experiment is conducted at $T = 6$ K to study polariton effects with decreased losses properly. According to our assumptions, the nanowire can be considered as a waveguide with quantized F-P resonances and also has to support exciton-polaritons. In this case, the observed ASE should turn to the lasing regime based on the F-P resonances. We synthesized lead-bromide perovskite nanowires (Fig. 2(f)) with a length of around 5 μm by the method mentioned in the Methods. At $T = 6$ K in a similar way to the previous experiment, we measure the emission from the nanowire under a femtosecond pump with angle resolution along the axis of the nanowire axis (Fig. 2(g–i)). At the low pump fluence, we observe only the spontaneous PL emission with uniform intensity distribution over the angle (Fig. 2(g)). With the increase of pump fluence after the threshold multimode lasing regime is achieved (Fig. 2(h)). The lasing emission has the checkerboard pattern in the angle dependence spectrum, which appears due to the interference of the coherent lasing emission, coming from two

edges of the nanowire, and it is discussed in detail in SI. With further increase of pump fluence, we observe strong red broadening of the lasing modes up to 100 meV (Fig. 2(i)), the same as for the 2D thin film guided-polariton ASE. The origin of the multimode lasing red broadening corresponds to the polariton relaxation and is discussed in the previous section.

Since there is no option to measure polariton dispersion in a perovskite nanowire properly and prove their existence experimentally, we study the free spectral range (FSR) of lasing peaks, obtained at pump fluence 850 μJ/cm^2. Thanks to the angle-resolved spectroscopy and checkerboard pattern we can better distinguish one mode from another. Based on the FSR we estimate the group refractive index that is rapidly increased up to the value of 45 near the exciton resonance (Fig. 2(h)), which points to the exciton-polariton origin of the lasing F-P resonances, observed before in ref.[43].

To obtain the 0D perovskite system with only a few Mie-polariton states, we prepare lead-bromide nanocuboids via modified hot-injection synthesis and further deposit on the metal-dielectric substrate by drop-casting (See *Methods* and Section 6 of SI for the details). In turn, the integration of semiconductors with plasmonic surfaces[62] or nanostructures[63] can be employed to tailor and enhance the optical response. The substrate with plasmonic effects acts as a mirror for certain Mie-modes of the nanoparticle, resulting in the enhancement of field localization and mode selectivity[62,64] (see Fig. S8 and S10 in SI). We perform the same emission measurements for the synthesized perovskite nanocuboid (Fig. 2(k)) with a physical volume of 0.02 μm^3 on the Al_2O_3/Ag/Si substrate, which supports few Mie-resonances in the spectral region near the exciton level. At the pump with fluences lower than 1 μJ/cm^2 the low-intensity linear PL spectrum is observed (Fig. 2(l)). At the pump threshold around 4 μJ/cm^2, narrow lasing peaks appear, corresponding to Modes 1 and 2 in Fig. 2(m). With increasing of pump fluence around 17 μJ/cm^2 the next Mode 3 appears with pronounced radiation patterns in the angle-resolved spectrum (Fig. 2(m)), which corresponds to the particular Mie-modes, discussed in SI, Fig. S3, and also in the next section.

The main difference between the 0D perovskite structure with 1D and 2D is in the dynamics of lasing peaks with increasing pump fluence. Instead of stimulated emission red broadening, we observe the blueshift and broadening of the lasing peaks (Fig. 2(n)). Exciton-polaritons cannot scatter to the lower energy states and therefore accumulate in the available lasing levels. Accumulated polaritons in the same quantum state start to interact with each other through Coulomb potential, which shifts polariton levels to the blue region[65,66].

The broadening of the lasing spectra in nanocuboids is suggested to have originated from two mechanisms. The first one is the aforementioned polariton-polariton interaction. The second can be caused by temporal broadening: pumping pulse excites a huge number of the polaritons, accumulated in the lasing state; polariton level shifts to the blue region because of the Coulomb interaction; accumulated polaritons fall to the ground state and produces narrow coherent polariton lasing emission; with the time the number of the polaritons in the lasing levels are reducing polariton lasing peak shifts to the red region but with continuing lasing emission. The recent work demonstrated the polariton lasing with the angular and temporal resolution, where this phenomenon is observed and confirmed[67]. As in the experiment, the measurements are performed with time integration, we observe only blueshift and broadening, however, previous studies have already observed the effect in the lead-bromide microlasers with time resolution[68].

Mie-resonances in perovskite nanocuboids strongly depend on the geometrical sizes and have no angular dispersion with the energy of thin film or nanowire. Therefore, we can only indirectly confirm the polariton origin of the Mie-modes by the calculation of eigenfrequencies of Mie-resonances with the account of the refractive index dispersion, affected by exciton resonance. The refractive index at cryogenic temperature is estimated based on the experimental micro-ellipsometry measurements[31] and reflectance spectra of lead-bromide thin nanoplates with different thicknesses measured at room temperature and 6 K (See Fig. S9 in SI for the details). We calculate the spectral position of the Mie-resonance as a function of the nanocuboid volume and compare it with the case when the refractive index is constant for all light wavelengths (See *Methods* for the details). As shown in Fig. 2(o), with reducing the active media volume the spectral position of the Mie-modes shifts toward the exciton asymptote. If we consider a constant refractive index without exciton resonance, the spectral position of the Mie-modes demonstrates almost linear dependence with the nanocuboid inverted volume. The difference between the two lines can be explained by the strong light-matter coupling regime of the Mie-resonances, cal-

culated with the material dispersion and exciton state. The modeling results together with the experimental study of lasing peaks evolution confirm the polariton origin of Mie-modes.

On one hand, the exciton-polariton nature of perovskite self-resonating cavities allows for realizing inversion-free coherent emission due to the boson stimulation. On the other hand, polariton relaxation leads to the red broadening of coherent emission. The latter does not allow the achievement of a single or few-mode lasing regime and also prevents effective polariton accumulation in a single state with narrow lasing emission. However, if we turn to the 0D structure, where there are no continuous polariton states and only discrete Mie resonances, the phenomenon of the stimulated emission red broadening disappears, while the inversion-free regime would remain. In the next sections, we represent the clear transition from the multi-mode lasing regime to the single-mode lasing in perovskite nanocuboid, show the analysis of the Mie-modes in perovskite nanocuboids, located on the plasmonic substrate, and study in detail the dynamics of the polariton emission.

Exciton-polariton lasing in nanocuboids

The number of the polariton Mie-resonances in the perovskite nancuboids is determined by their sizes. Thus, we synthesize nanocuboids with different sizes during the study (See *Methods* and Fig. S7 in SI for the details), and choose the most relevant volumes (0.37 μm^3, 0.02 μm^3 and 0.007 μm^3) which demonstrate multimode lasing, few-mode lasing, and single-mode lasing regimes, respectively (See Fig. 3(g–j)).

With the increase in the pump fluence, the nanocuboid with the largest volume of 0.37 μm^3 (Fig. 3(a)) leads to multi-mode lasing accompanied by red broadening (Fig. 3(d)), which corresponds to the similar polariton relaxation phenomenon, discussed above with 1D and 2D structures (Fig. 2(i)). The large mode volume of the cuboid provides the numerous discrete Mie-states through which the stimulated polariton relaxation occurs. The mechanism for fluence-driven red broadening involves an increase in the number of phonons taking part in the polariton relaxation, resulting in the saturation of high-frequency modes and ascending of low-frequency ones. For 0.37 μm^3 cuboid, such a trend is vividly presented by the laser intensity dependency on fluence for every mode (Fig. 3(d)).

However, the spectral dynamic drastically changes with a decrease in the cuboid size. We conduct the same measurements with 0.02 μm^3 cuboid, revealing lasing only on three modes according to experimental observations. The first mode appears upon excitation fluence around 1 μJ/cm^2, pointing out the inversion-free regime. With an increase in the pump fluence, two additional channels of polariton relaxation towards the second and third Mie-modes appear at ~ 4 μJ/cm^2 and ~ 17 μJ/cm^2, respectively (Fig. 3(e)). Further polariton thermalization is not observed, due to the large energy gap, exceeding phonon energies, or insufficient Q-factor of low-energy modes. Therefore, polaritons accumulate at three Mie-energy levels ($E_3 > E_2 > E_1$), resulting in polariton-polariton interaction through Coulomb potential and strong blueshift at the higher excitation fluence (F > 100 μJ/cm^2)[69]. This nonlinear regime is shown by empty circles in the mode intensity plot as a function of the pump fluence in Fig. 3(h).

Notably, the pump fluence saturation for the higher energy mode (E_2) corresponds to the threshold fluence for the lower energy one (E_1). In accordance with the model based on coupled rate equations discussed above, the stimulated polariton relaxation provides the lasing at the E_1 level, when the nonlinear term of the relaxation to this level exceeds the rate of the annihilation. This in turn leads to the scenario when the particles at the E_2 level rather scatter to the lower state E_1 than radiatively annihilate at the E_2 level. Therefore, the lasing intensity of the second mode does not rise, when the stimulated relaxation channel for the first mode is opened. The hypothesis is supported by the results of calculations using the theoretical model described in the previous section, which are shown in Fig. 3(h) as dashed lines and well match with the experimental results.

Encouraged by these findings we aim at the major challenge for the creation of the single-mode polariton laser having the smallest physical volume ever and operating upon an inversion-free regime. We study a cuboid with a physical volume around 0.007 μm^3 (Fig. 3(c)) exhibiting completely suppressed polariton relaxation. It is established that laser generation occurs at an electric quadrupole Mie-mode at ~ 2 μJ/cm^2 (Fig. 3(f, j)), accompanied by a narrowing of the full width at half-maximum (FWHM) to ~ 0.6 nm (Fig. S15). As expected, this cuboid demonstrates only the blueshift of laser emission because of the polariton accumulation at a single Mie-energy level.

The dominating quadrupole nature of single lasing

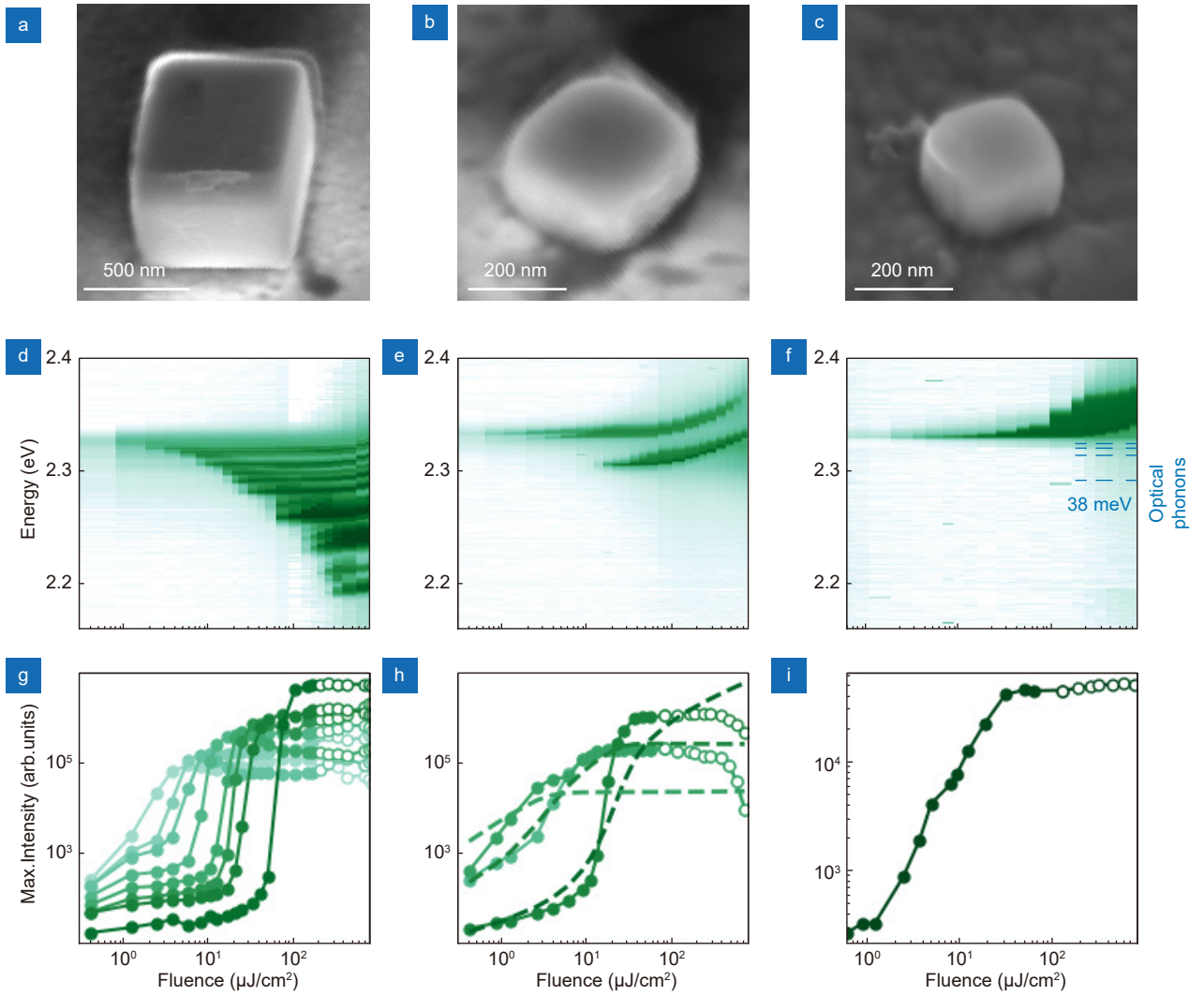

Fig. 3 | Lasing emission measurements of perovskite nanocuboids with different sizes. (**a–c**) SEM images of studied perovskite nanocuboids with different geometry. The physical volume of the cuboids is 0.37, 0.02, and 0.007 μm³ respectively. (**d–f**) Emission spectra as a function of the pump fluence obtained at 6 K for respective samples are shown below in (a–c). Intensive peaks in the spectra correspond to the lasing emission. Dashed blue lines in (**f**) correspond to phonon energies shifted from the spectral center of the lasing mode. (**g–j**) The intensity of the lasing peaks, shown in (d–f) as a function of the pump fluence. Dashed lines in (**h**) correspond to the results of the theoretical model of the polariton lasing and phonon relaxation in perovskite nanocuboid based on Eq. (1).

mode was confirmed by rigorous eigenmode analysis using Commercial Software COMSOL Multiphysics (See *Methods* and Fig. S10 in SI for details). Numerical analysis reveals that the smallest cuboid on a metal-dielectric substrate possesses a relatively high *Q*-factor for the resonance ($Q \sim 68$) hybrid Mie-mode at 2.33 eV, where the main contribution to mode field localization is governed by electric quadrupole with an azimuthal number $m = 2$ (further refereed as EQ) (Fig. 4(a)). We experimentally measure the angle-resolved emission of the smallest cuboid above the lasing threshold indicating that the radiation has a pronounced directivity within a solid angle defined by $NA = 0.55$ of a 50× objective lens, which at the normal direction the emission intensity tends to zero (Fig. 4(b)). The obtained result is plotted in polar coordinates (orange dots in Fig. 4(c)) and consistent with the directivity of EQ (orange dashed curves in Fig. 4(c)) in Fig. 4(a). Therefore, both the spectral position and directivity of the calculated eigenmode agree well with the experimental observations, which points out the correct identification of the laser mode. A similar analysis is also performed for the middle-sized cuboid (Fig. 3(b)), where mode with $Q_1 \sim 59$ and $Q_2 \sim 60$ correspond to non-degenerated (because of unequal sides) hybrid mode, while the lower energy Mie-mode has $Q_3 \sim 57.8$ with the major contribution from magnetic

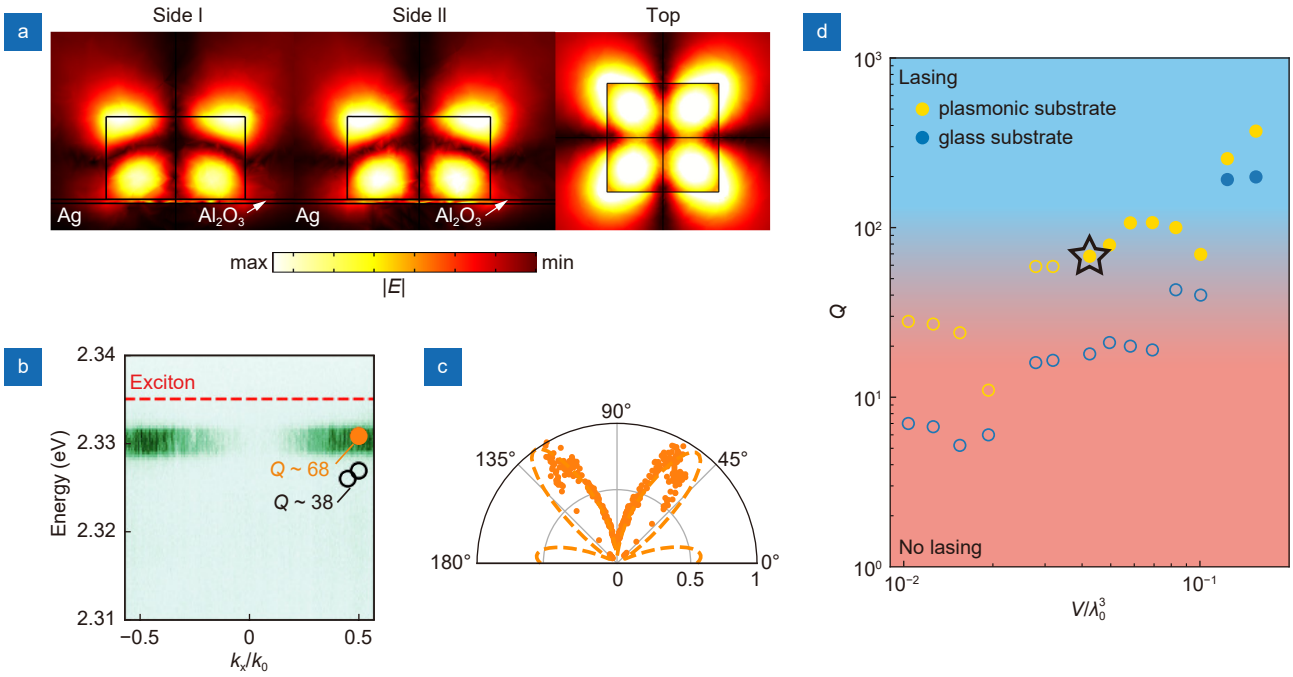

Fig. 4 | Analysis of the Mie-mode observed in the smallest perovskite nanocuboid. (**a–c**) Identification of the laser mode in cuboid with the smallest physical volume V = 0.007 μm³ (0.04 λ_0^3, where λ_0 = 0.53 μm) (SEM image in Fig. 3(c)), providing the single mode lasing as shown in Fig. 3(f, j). (a) Electric field distribution of the identified electric quadrupole (EQ) mode in three cross-sections. (b) Angle-resolved spectrum obtained at fluence around 10 μJ/cm². The presented laser line at 2.33 eV occurs at EQ resonance with Q ~ 68 (shown by the orange circle) with field localization shown in (a). The dashed red line corresponds to the exciton energy level, while empty black circles denote two more low-Q modes, presenting in this cuboid, but insufficient for lasing. (c) Angle-resolved spectrum in (b), plotted in polar coordinates (orange dots), and numerical simulated directivity (dashed orange curve), obtained in the far-field of EQ eigenmode (a). (**d**) The highest quality factor, Q, presenting in cuboid on metal-dielectric (yellow dots) and glass (blue dots) substrates versus normalized cuboid volume, V/λ_0^3. Here, the gradual transition defines the threshold level required for laser generation, obtained from a semiempirical approach, whereas modes under threshold are denoted by empty circles for clarity. The black star corresponds to the smallest laser achieved in this work, having a physical volume V = 0.007 μm³ (0.047 λ_0^3, where λ_0 = 0.53 μm) (see SEM image in Fig. 3(c)).

quadrupole with the azimuthal number m = 2 (Fig. S3).

Interestingly, pumping the nanocuboids with a physical volume smaller than 0.007 μm³ (0.04 λ_0^3, where λ_0 = 0.53 μm) gives no lasing. To clarify this, the threshold radiative Q-factor required for lasing is identified to be around 52 on the basis of consistent data derived from experimentally observable laser modes and numerical modeling for corresponding eigenmodes. According to the defined threshold depicted in Fig. 4(d) as the gradual transition, cuboids on the plasmonic substrate (green circles) that have a value V/λ_0^3 less than 0.04 (signed with a star), apparently, are not capable of exhibiting lasing because of insufficient Q-factor. In turn, glass substrate does not afford laser generation in nanocuboids (blue circles) with V/λ_0^3 up to 0.12. Therefore, we promote the utilization of the metal-dielectric substrate providing the most compact laser semiconductor cavities with both efficient cooling and selective enhancement of certain Mie-modes (See Fig. S8 in SI)[64,78]. In the case of the studied EQ mode in the nanocuboid mentioned above, coupling to mirroring plasmonic substrate leads to an almost 7 times increase in Q-factor in comparison with the same cuboid on glass, where a substantial mode leakage takes place (Fig. S10). Complementary experimental evidence of field localization enhancement provided by plasmonic substrate could be an observed acceleration of photoluminescence decay in the nanocuboid on the plasmonic substrate, as compared to that for similar cuboid on the glass substrate due to the Purcell effect (Fig. S11).

To assess the contribution of our design to the concept of semiconductor laser medium miniaturization for the creation of building blocks in integrated photonic devices, we compare its physical and normalized volume as well as basic laser characteristics with those of other similar micro/nano lasers, operating in various spectral ranges (Table S1). As demonstrated in many compact perovskite designs, the color tunability by changing halogen at "X" site allows to easily obtain lasers in the whole

visible spectral range with normalized volume, V/λ^3, close to 1 (Fig. 5(a)). One of the most efficient strategies to push the compactness limit further is the integration of a perovskite cavity with a metal-dielectric substrate, which was demonstrated by ref.[73,76]. Remarkable progress in laser miniaturization is obtained with transition from a nanowire towards a nanocuboid of the most structurally stable composition $CsPbBr_3$ (Fig. 5(a)). Over the past decade, the size of "green" perovskite lasers has dropped down more than 2 orders of magnitude in terms of V/λ^3 (Fig. 5(b)). In this work, we integrate the smallest perovskite cavity ($V/\lambda^3 \sim 0.04$) with the metal-dielectric substrate yielding 5 times decrease in size as compared to the previous best result $V/\lambda^3 \sim 0.2$[75]. Thus the produced single-mode Mie-polariton nanolaser sets a new record for miniature perovskite lasers (Fig. 5(a, b)), providing them with the niche among the most compact semiconductor designs (Table S1).

Conclusion

To conclude, we have proposed a strategy to create ultra-small nanolasers and proved it experimentally. Namely, it is essential to create a cavity from the light-emitting material satisfying the following conditions: a high refractive index for modes localization in the nanocavity, a high binding energy and oscillator strength of the exciton to achieve polariton lasing, and a high quantum yield or luminescence to avoid overheating, as well as low phonon energies to prevent parasitic relaxation of exciton-polariton to lower states. We have supported this statement by rigorous experimental study of lead-bromide perovskite 0D cavity (nanocuboids) as well as for 1D and 2D cavities (nanowires and films). We have revealed that $CsPbBr_3$ perovskite is a promising material platform for the creation of ultra-small lasers, because of the high binding energy of exciton (35 meV), high refractive index near the exciton (>2.5), high quantum yield, and heavy ions resulting in low energies of optical phonons (<40 meV) being less than the intermodal spectral distance in a small Mie-resonant nanocavity.

As a result of the optical design optimization, we have achieved exciton-polariton lasing at low temperature in the nanocuboid laser based on the second-order Mie resonance with Q-factor significantly enhanced by a metallic substrate, which allows us to achieve the smallest volume $(\lambda/2.7)^3$ among all perovskite lasers reported so

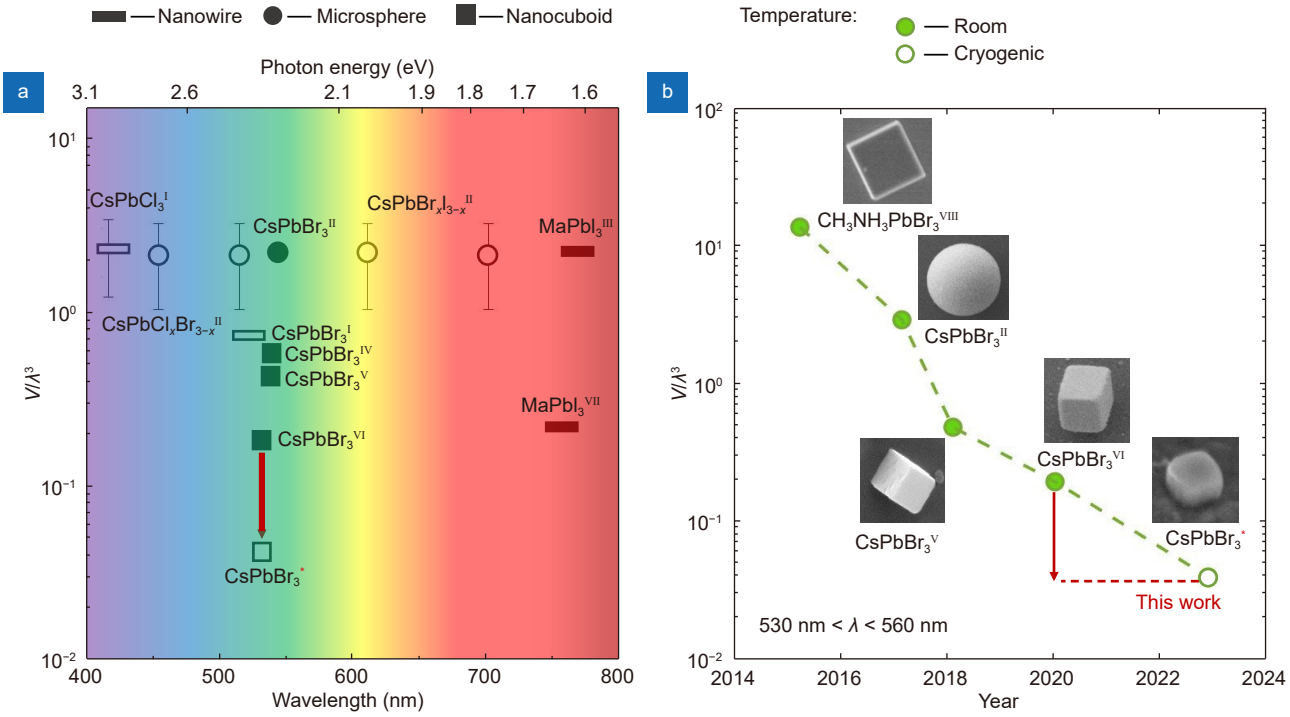

Fig. 5 | Comparison of the smallest perovskite polariton nanolaser with previous reports. (**a**) Reported perovskite laser designs (nanowire, microsphere, and cuboids) having small normalized volumes, V/λ^3, with lasing wavelength over the whole VIS range at room (filled marker) and cryogenic (empty marker) temperatures. (**b**) Normalized volume versus year showing the status of green light emitting perovskite nanolasers miniaturization. Data were adapted from the following references: I[70]; II[71]; III[72]; IV[73]; V[74]; VI[75]; VII[76]; VIII[77]. The red arrow indicates progress achieved in this work.

far[75]. Moreover, the nanolaser works at a very low threshold 2 μJ/cm^2 caused by the inversion-free nature of the emission. Moreover, the developed method for colloidal synthesis of nanocuboid particles allows for the simple deposition of nanolasers, which makes it suitable for simple integration with various photonic circuits or conductive substrates, being also promising for electrically driven nanolasers in the visible range. Further progress in the fabrication of polariton nanolasers can be attributed to the implementation of template-assisted synthesis, which allows precise control of spatial position and size[79,80]. Additionally, the transition from noble metals to more affordable materials such as aluminum would be worthwhile.

Methods

Film synthesis

$MAPbBr_3$ thin film was synthesized by the spin-coating method[81]. Perovskite solution was prepared in the nitrogen dry box by mixing 56.0 mg of methylammonium bromide (MABr) from GreatCell Solar and 183.5 mg of Lead(II) bromide ($PbBr_2$) from TCI in the glass vial. Salts were dissolved in 1 mL of DMF:DMSO solvent mixture in the ratio 3:1. Obtained $MAPbBr_3$ solution with 0.5M molarity was stirred for 1 day at 27 °C.

We used SiO_2 substrates (12.5 × 12.5 mm^2), which were washed with sonication in the deionized water, acetone, and 2-propanol for 10 min consecutively, and afterward cleaned in an oxygen plasma cleaner for 10 min. Prepared substrate transfer to the dry nitrogen glovebox for further spin-coating.

First, the substrate was located on the spin-coater and fixed by a vacuum pump, then 30 μL of the $MAPbBr_3$ solution was deposited on the top of the substrate, and after the substrate was spun at 3000 rpm for 40 s. At the 25 s 300 μL of toluene was dripped on the top of the rotating substrate to rapidly wash out the solvent and trigger the crystallization. After the spincoating substrates with perovskite film were annealed at 90 °C for 10 min.

Perovskite nanowire synthesis

Perovskite nanowire synthesis was performed by the developed solution-engineering method[61]. First, $CsPbBr_3$ solution was prepared: 110 mg of $PbBr_2$ and 63 mg of CsBr from TCI were dissolved in 3 mL of DMSO by shaking for 10 min to afford a clear solution in a dry nitrogen glovebox atmosphere. Glass substrates were cleaned at ambient conditions with chromium oxide paste and rinsed with distilled water to ensure the hydrophobic surface. The prepared perovskite solution was taken out from the glovebox, exposed to the 30% humid air, and kept in the closed vial for 15 min. Then 20 μL of the solution was deposited on the rotating substrate at 2000 rpm for 30 s. After the sample was put in a small plastic Petri dish bottom (35 × 9 mm^2) placed in a bigger glass one (80 × 15 mm^2). The whole system was heated up to 50 °C and 200 μL of IPA·H_2O azeotrope was poured into the glass Petri and all the system was capped with a glass Petri top. At the final stage, the sample was annealed in the system at 50 °C for 6 min in the presence of 2-propanol-water azeotropic vapor.

Perovskite nanocube synthesis

The following protocol reproducing a hot-injection method[29] adapted to the synthesis of perovskite Mie-resonance nanocuboids was employed. First, cesium oleate (CsOA) in 1-octadecene (ODE) 0.125 M solution was prepared. For this, 2.5 mmol of Cs_2CO_3 was loaded in a flask containing 40 mL of ODE and stirred (1000 rpm) at 140 °C in a N_2-filled glovebox for 1 h followed by its reaction with 5 mmol of oleic acid (OA) giving a clear solution that turns to be milky at room temperature. The solution was stored in the glovebox and preheated before the hot-injection procedure. Second, 0.2 mmol of $PbBr_2$ was stirred (1000 rpm) in 5 mL of ODE in a vacuumized two-neck round-bottom flask (50 mL) at 120 °C for 1 h. Thereafter, the flask was filled in with N_2 gas, heated up to 140 °C, and 0.4 mmol of oleylamine (OLAm) and 0.4 mmol of OA were consequently added dropwise to completely dissolve lead bromide powder. Then, a clear solution was heated up to 180 °C followed by a rapid injection of 0.05 mmol of CsOA in ODE solution. The reaction mixture was stirred at 180 °C for 10 min and was quenched in an ice bath afterward. The obtained suspension was centrifuged at 500 rpm for 5 min. A supernatant containing small perovskite nanocrystals was discarded. A precipitate was redispersed in 10 mL of toluene. The suspension was left for 20 min to let the Mie-resonance nanocuboids settle out. Finally, the supernatant was pipetted out and the sediment was redispersed in 10 mL of n-hexane for further utilization.

Metal-dielectric Al_2O_3/Ag/Si substrates were fabricated by using the following approach. First, Ag film with a thickness of 50 nm was deposited on Si substrates at 0.2 A/s rate by thermo-resistive evaporation in a vacuum

chamber (Nanovak) at 2×10^{-6} torr pressure (1 torr ≈ 1.33 × 10^2 Pa). Thereafter, the resultant Ag/Si samples were coated with 6 nm layer of amorphous aluminum oxide produced by atomic layer deposition (ALD) using $Al_2(CH_3)_6$ (trimethylaluminium) and H_2O as precursors. 60-cycle deposition was conducted at 300 °C and coating rate 1.05 A/cycle on Cambridge NanoTech Savannah Atomic Layer Deposition System. The AFM image of the substrate surface was obtained on AIST SmartSPM 1000 atomic force microscopy (See Fig. S6 in SI for details).

Suspension of $CsPbBr_3$ nanocuboids in n-hexane was dropcasted on metal-dielectric and glass substrates for carrying out optical experiments.The morphology and size of the nanocuboids were studied using Zeiss Neon 40 and Zeiss Merlin scanning electron microscopes.

Optical measurements

Pump-dependent emission spectra with angular distribution were obtained by a back-focal-plane setup with a slit spectrometer coupled to a liquid-nitrogen-cooled imaging CCD camera (Princeton Instruments SP2500+PyLoN). Femtosecond (fs) laser (Pharos, Light Conversion) coupled with a broad-bandwidth optical parametric amplifier (Orpheus-F, Light Conversion) was used as a pump for the PL excitation at the wavelength of 490 nm with a repetition rate of 100 kHz. Both for the focusing of the laser beam and for collecting the emission signal infinity-corrected objective (Mitutoyo 50× NIR HR with *NA* = 0.65) was used. Samples were placed in a closed-cycle helium cryostat (Advanced Research Systems) and maintained at a controllable temperature in the range of 7–300 K. The spatial filter was used to get rid of parasitic signals from the neighborhood nanocrystals and reflections from the optical elements in the setup.

Time-resolved measurements at room and cryogenic temperatures were carried out using a PicoHarp 300 TCSPC module (PicoQuant). A femtosecond laser (Pharos, Light Conversion) coupled with a broad-bandwidth optical parametric amplifier (Orpheus-F, Light Conversion) was used as a pump source (λ_{ex} = 490 nm, *RR* = 100 kHz, $\tau \approx$ 220 fs). The laser beam was focused on the sample surface, and placed in a closed-cycle helium cryostat, at normal incidence by an infinity-corrected objective (Mitutoyo 50× NIR HR *NA* = 0.65) providing the sample with uniform irradiation (Gaussian distribution with FWHM of ≈ 10 μm). Spontaneous PL emission was collected by the same objective and sent towards a photon counting detector module (photon timing resolution of 50 ps (FWHM), PDM Series, Micro Photon Devices). To get rid of residual excitation light the longpass filter with cut-on wavelength 500 nm (FELH0500, Thorlabs) was used. The spatial filter was used to get rid of parasitic signals from the neighborhood nanocrystals and reflections from the optical elements in the setup.

For the angle-resolved measurements of the perovskite film guided mode below the light line ($k_x/k_0 > 1$) ZnSe solid immersion lens (SIL) was used[82]. The flat side of the SIL was placed close to the thin film to the distances in the order of 100 nm by a hand-made setup with a piezo positioner. Infinity-corrected objective (Mitutoyo 100× HR VIS 0.9 *NA*) was focused through the SIL. The resulting NA of the system becomes equal to $NA = 0.9 \cdot n_{ZnSe} \approx 2.4$ in the studied spectral range. The collected signal from the SIL setup was transmitted to the mentioned back-focal-plane setup to get angle-resolved spectra. For the reflectance spectra halogen lamp was used, and for the pump-dependent PL spectra fs laser (Pharos, Light Conversion) at 515 nm with a 100 kHz repetition rate was used.

Fitting of guided polariton dispersion in thin film

To fit the polariton branch we take a particular spectrum for each measured available k_x/k_0 in the range from 1.65 to 1.9, shown in Fig. 2(e) and fit experimental data by the Lorentz peak function. Taking the center of the Lorentz peak function as a function of k_x/k_0 we obtain the experimental lower polariton dispersion.

In the current design, there is no upper polariton branch because of huge absorption above exciton resonance, therefore we can estimate Rabi splitting and light-matter coupling coefficient by two coupled oscillator models, using only lower polariton branch[58]. According to the model lower polariton can be described as:

$$E_{LP}(k) = \frac{\widetilde{E}_X + \widetilde{E}_C(k)}{2} - \frac{1}{2}\sqrt{(\widetilde{E}_C(k) - \widetilde{E}_X)^2 + 4g_0^2}\,, \quad (2)$$

where $E_{LP}(k)$ is lower polariton dispersion, $\widetilde{E}_X$ and $\widetilde{E}_C(k)$ is complex energy of exciton and uncoupled cavity photon respectively, g_0 is the light-matter coupling strength. Exciton level was estimated from PL and reflection spectra, and uncoupled cavity photon dispersion is linearly approximated in the spectral range far from exciton. By optimizing the parameter Ω_0 we fit experimental dispersion by the current model. Resulting real part of E_{LP} is shown in Fig. 2(e).

Mode analysis

Mode analysis of lasing in $CsPbBr_3$ cuboids at cryogenic temperature was performed in the frequency domain module of the COMSOL Multiphysics software package. Eigenfrequencies study was used to carry out the eigenmode calculation for the cavity with real geometrical parameters estimated from SEM image, and radiation patterns of eigenmodes were calculated using far-field domains. The surrounding area of the perovskite nanocuboid was simulated as a hemisphere of air (n = 1) with a radius of 1 μm with the outer perfectly matched layer. Following material parameters were employed: complex refractive index of $CsPbBr_3$ at ~6 K, calculated by analytical approach (See Section S7 of SI for more details), whereas optical constants for metal-dielectric substrate Ag, Al_2O_3 were taken from ref.[83,84], respectively. A constant refractive index of $CsPbBr_3$, n = 2.3, was used for carrying out the comparison with the case when the refractive index is constant for all light wavelengths.

References

1. Tatum JA, Gazula D, Graham L et al. VCSEL-based interconnects for current and future data centers. *J Light Technol* **33**, 727–732 (2015).
2. Smit M, van der Tol J, Hill M. Moore's law in photonics. *Laser Photonics Rev* **6**, 1–13 (2012).
3. Agrell E, Karlsson M, Chraplyvy AR et al. Roadmap of optical communications. *J Opt* **18**, 063002 (2016).
4. Ma RM, Ota S, Li YM et al. Explosives detection in a lasing plasmon nanocavity. *Nat Nanotechnol* **9**, 600–604 (2014).
5. Ma RM, Oulton RF. Applications of nanolasers. *Nat Nanotechnol* **14**, 12–22 (2019).
6. Liang Y, Li C, Huang YZ et al. Plasmonic nanolasers in on-chip light sources: prospects and challenges. *ACS Nano* **14**, 14375–14390 (2020).
7. McCall SL, Levi AFJ, Slusher RE et al. Whispering-gallery mode microdisk lasers. *Appl Phys Lett* **60**, 289–291 (1992).
8. Painter O, Lee RK, Scherer A et al. Two-dimensional photonic band-gap defect mode laser. *Science* **284**, 1819–1821 (1999).
9. Johnson JC, Yan HQ, Schaller RD et al. Single nanowire lasers. *J Phys Chem B* **105**, 11387–11390 (2001).
10. Azzam SI, Kildishev AV, Ma RM et al. Ten years of spasers and plasmonic nanolasers. *Light Sci Appl* **9**, 90 (2020).
11. Hill MT, Gather MC. Advances in small lasers. *Nat Photonics* **8**, 908–918 (2014).
12. Ha ST, Fu YH, Emani NK et al. Directional lasing in resonant semiconductor nanoantenna arrays. *Nat Nanotechnol* **13**, 1042–1047 (2018).
13. Kodigala A, Lepetit T, Gu Q et al. Lasing action from photonic bound states in continuum. *Nature* **541**, 196–199 (2017).
14. Mylnikov V, Ha ST, Pan ZY et al. Lasing action in single subwavelength particles supporting supercavity modes. *ACS Nano* **14**, 7338–7346 (2020).
15. Wu MF, Ding L, Sabatini RP et al. Bound state in the continuum in nanoantenna-coupled slab waveguide enables low-threshold quantum-dot lasing. *Nano Lett* **21**, 9754–9760 (2021).
16. Tripathi A, Kim HR, Tonkaev P et al. Lasing action from anapole metasurfaces. *Nano Lett* **21**, 6563–6568 (2021).
17. Hwang MS, Lee HC, Kim KH et al. Ultralow-threshold laser using super-bound states in the continuum. *Nat Commun* **12**, 4135 (2021).
18. Sung J, Shin D, Cho H et al. Room-temperature continuous-wave indirect-bandgap transition lasing in an ultra-thin WS_2 disk. *Nat Photonics* **16**, 792–797 (2022).
19. Nezhad MP, Simic A, Bondarenko O et al. Room-temperature subwavelength metallo-dielectric lasers. *Nat Photonics* **4**, 395–399 (2010).
20. Khajavikhan M, Simic A, Katz M et al. Thresholdless nanoscale coaxial lasers. *Nature* **482**, 204–207 (2012).
21. Ding K, Ning CZ. Metallic subwavelength-cavity semiconductor nanolasers. *Light Sci Appl* **1**, e20 (2012).
22. Polushkin AS, Tiguntseva EY, Pushkarev AP et al. Single-particle perovskite lasers: from material properties to cavity design. *Nanophotonics* **9**, 599–610 (2020).
23. Byrnes T, Kim NY, Yamamoto Y. Exciton-polariton condensates. *Nat Phys* **10**, 803–813 (2014).
24. Imamou A, Ram RJ, Pau S et al. Nonequilibrium condensates and lasers without inversion: exciton-polariton lasers. *Phys Rev A* **53**, 4250–4253 (1996).
25. Kasprzak J, Richard M, Kundermann S et al. Bose-Einstein condensation of exciton polaritons. *Nature* **443**, 409–414 (2006).
26. Deng H, Weihs G, Snoke D et al. Polariton lasing vs. photon lasing in a semiconductor microcavity. *Proc Natl Acad Sci USA* **100**, 15318–15323 (2003).
27. Di Stasio F, Christodoulou S, Huo NJ et al. Near-unity photoluminescence quantum yield in $CsPbBr_3$ nanocrystal solid-state films via postsynthesis treatment with lead bromide. *Chem Mater* **29**, 7663–7667 (2017).
28. Kang J, Wang LW. High defect tolerance in lead halide perovskite $CsPbBr_3$. *J Phys Chem Lett* **8**, 489–493 (2017).
29. Protesescu L, Yakunin S, Bodnarchuk MI et al. Nanocrystals of cesium lead halide perovskites ($CsPbX_3$, X= Cl, Br, and I): novel optoelectronic materials showing bright emission with wide color gamut. *Nano Lett* **15**, 3692–3696 (2015).
30. Baranowski M, Plochocka P. Excitons in metal-halide perovskites. *Adv Energy Mater* **10**, 1903659 (2020).
31. Ermolaev G, Pushkarev AP, Zhizhchenko A et al. Giant and tunable excitonic optical anisotropy in single-crystal halide perovskites. *Nano Lett* **23**, 2570–2577 (2023).
32. Tatarinov DA, Anoshkin SS, Tsibizov IV et al. High-quality $CsPbBr_3$ perovskite films with modal gain above 10 000 cm^{-1} at room temperature. *Adv Opt Mater* **11**, 2202407 (2023).
33. Huang C, Zhang C, Xiao SM et al. Ultrafast control of vortex microlasers. *Science* **367**, 1018–1021 (2020).
34. Evans TJS, Schlaus A, Fu YP et al. Continuous-wave lasing in cesium lead bromide perovskite nanowires. *Adv Opt Mater* **6**, 1700982 (2018).
35. Tao RJ, Peng K, Haeberlé L et al. Halide perovskites enable polaritonic *XY* spin hamiltonian at room temperature. *Nat Mater* **21**, 761–766 (2022).
36. Su R, Ghosh S, Wang J et al. Observation of exciton polariton condensation in a perovskite lattice at room temperature. *Nat Phys* **16**, 301–306 (2020).
37. Su R, Fieramosca A, Zhang Q et al. Perovskite semiconductors

for room-temperature exciton-polaritonics. *Nat Mater* **20**, 1315–1324 (2021).
38. Wu JQ, Ghosh S, Su R et al. Nonlinear parametric scattering of exciton polaritons in perovskite microcavities. *Nano Lett* **21**, 3120–3126 (2021).
39. Feng JG, Wang J, Fieramosca A et al. All-optical switching based on interacting exciton polaritons in self-assembled perovskite microwires. *Sci Adv* **7**, eabj6627 (2021).
40. Li Y, Ma XK, Zhai XK et al. Manipulating polariton condensates by Rashba-Dresselhaus coupling at room temperature. *Nat Commun* **13**, 3785 (2022).
41. Zhao Z, Zhong MY, Zhou WC et al. Simultaneous triplet exciton-phonon and exciton-photon photoluminescence in the individual weak confinement $CsPbBr_3$ micro/nanowires. *J Phys Chem C* **123**, 25349–25358 (2019).
42. Sich M, Krizhanovskii DN, Skolnick MS et al. Observation of bright polariton solitons in a semiconductor microcavity. *Nat Photonics* **6**, 50–55 (2012).
43. Shang QY, Li ML, Zhao LY et al. Role of the exciton-polariton in a continuous-wave optically pumped $CsPbBr_3$ perovskite laser. *Nano Lett* **20**, 6636–6643 (2020).
44. Wang SJ, Raziman TV, Murai S et al. Collective mie exciton-polaritons in an atomically thin semiconductor. *J Phys Chem C* **124**, 19196–19203 (2020).
45. Deng H, Haug H, Yamamoto Y. Exciton-polariton Bose-Einstein condensation. *Rev Mod Phys* **82**, 1489–1537 (2010).
46. Shan HY, Iorsh I, Han B et al. Brightening of a dark monolayer semiconductor via strong light-matter coupling in a cavity. *Nat Commun* **13**, 3001 (2022).
47. Zhou XZ, Zhang ZY. Electron-phonon coupling in $CsPbBr_3$. *AIP Adv* **10**, 125015 (2020).
48. Chen ST, Nurmikko A. Excitonic gain and laser emission from mixed-cation halide perovskite thin films. *Optica* **5**, 1141–1149 (2018).
49. Kavokin A, Baumberg JJ, Malpuech G et al. *Microcavities* 2nd ed (Oxford University Press, Oxford, 2017).
50. Piermarocchi C, Tassone F, Savona V et al. Nonequilibrium dynamics of free quantum-well excitons in time-resolved photoluminescence. *Phys Rev B* **53**, 15834–15841 (1996).
51. Tassone F, Yamamoto Y. Exciton-exciton scattering dynamics in a semiconductor microcavity and stimulated scattering into polaritons. *Phys Rev B* **59**, 10830–10842 (1999).
52. Saba M, Quochi F, Mura A et al. Excited state properties of hybrid perovskites. *Acc Chem Res* **49**, 166–173 (2016).
53. Ryu H, Byun HR, McCall KM et al. Role of the A-site cation in low-temperature optical behaviors of $APbBr_3$ (A = Cs, CH_3NH_3). *J Am Chem Soc* **143**, 2340–2347 (2021).
54. Enomoto S, Tagami T, Ueda Y et al. Drastic transitions of excited state and coupling regime in all-inorganic perovskite microcavities characterized by exciton/Plasmon hybrid natures. *Light Sci Appl* **11**, 8 (2022).
55. Klimov VI, Mikhailovsky AA, Xu S et al. Optical gain and stimulated emission in nanocrystal quantum dots. *Science* **290**, 314–317 (2000).
56. Hofmann MR, Gerhardt N, Wagner AM et al. Emission dynamics and optical gain of 1.3-/spl mu/m (GaIn)(NAs)/GaAs lasers. *IEEE J Quantum Electron* **38**, 213–221 (2002).
57. Geiregat P, Maes J, Chen K et al. Using bulk-like nanocrystals to probe intrinsic optical gain characteristics of inorganic lead halide perovskites. *ACS Nano* **12**, 10178–10188 (2018).
58. Hopfield JJ. Theory of the contribution of excitons to the complex dielectric constant of crystals. *Phys Rev* **112**, 1555–1567 (1958).
59. Khmelevskaia D, Markina D, Tonkaev P et al. Excitonic versus free-carrier contributions to the nonlinearly excited photoluminescence in $CsPbBr_3$ perovskites. *ACS Photonics* **9**, 179–189 (2021).
60. Masharin MA, Shahnazaryan VA, Iorsh IV et al. Room-temperature polaron-mediated polariton nonlinearity in $MAPbBr_3$ perovskites. *ACS Photonics* **10**, 691–698 (2023).
61. Pushkarev AP, Korolev VI, Markina DI et al. A few-minute synthesis of $CsPbBr_3$ nanolasers with a high quality factor by spraying at ambient conditions. *ACS Appl Mater Interfaces* **11**, 1040–1048 (2019).
62. Markovich DL, Ginzburg P, Samusev AK et al. Magnetic dipole radiation tailored by substrates: numerical investigation. *Opt Express* **22**, 10693–10702 (2014).
63. Nevet A, Berkovitch N, Hayat A et al. Plasmonic nanoantennas for broad-band enhancement of two-photon emission from semiconductors. *Nano Lett* **10**, 1848–1852 (2010).
64. Sinev I, Iorsh I, Bogdanov A et al. Polarization control over electric and magnetic dipole resonances of dielectric nanoparticles on metallic films. *Laser Photonics Rev* **10**, 799–806 (2016).
65. Bajoni D, Senellart P, Wertz E et al. Polariton laser using single micropillar GaAs-GaAlAs semiconductor cavities. *Phys Rev Lett* **100**, 047401 (2008).
66. Gao T, Eldridge PS, Liew TCH et al. Polariton condensate transistor switch. *Phys Rev B* **85**, 235102 (2012).
67. Ardizzone V, Riminucci F, Zanotti S et al. Polariton Bose-Einstein condensate from a bound state in the continuum. *Nature* **605**, 447–452 (2022).
68. Schlaus AP, Spencer MS, Miyata K et al. How lasing happens in $CsPbBr_3$ perovskite nanowires. *Nat Commun* **10**, 265 (2019).
69. Masharin MA, Shahnazaryan VA, Benimetskiy FA et al. Polaron-enhanced polariton nonlinearity in lead halide perovskites. *Nano Lett* **22**, 9092–9099 (2022).
70. Jiang L, Liu RM, Su RL et al. Continuous wave pumped single-mode nanolasers in inorganic perovskites with robust stability and high quantum yield. *Nanoscale* **10**, 13565–13571 (2018).
71. Tang B, Dong HX, Sun LX et al. Single-mode lasers based on cesium lead halide perovskite submicron spheres. *ACS Nano* **11**, 10681–10688 (2017).
72. Zhu HM, Fu YP, Meng F et al. Lead halide perovskite nanowire lasers with low lasing thresholds and high quality factors. *Nat Mater* **14**, 636–642 (2015).
73. Cho S, Yang Y, Soljačić M et al. Submicrometer perovskite plasmonic lasers at room temperature. *Sci Adv* **7**, eabf3362 (2021).
74. Liu ZZ, Yang J, Du J et al. Robust subwavelength single-mode perovskite nanocuboid laser. *ACS Nano* **12**, 5923–5931 (2018).
75. Tiguntseva E, Koshelev K, Furasova A et al. Room-temperature lasing from Mie-resonant nonplasmonic nanoparticles. *ACS Nano* **14**, 8149–8156 (2020).
76. Yu HC, Ren KK, Wu Q et al. Organic-inorganic perovskite plasmonic nanowire lasers with a low threshold and a good thermal stability. *Nanoscale* **8**, 19536–19540 (2016).
77. Liao Q, Hu K, Zhang HH et al. Perovskite microdisk microlasers self-assembled from solution. *Adv Mater* **27**, 3405–3410 (2015).
78. Xifré-Pérez E, Shi L, Tuzer U et al. Mirror-image-induced magnetic modes. *ACS Nano* **7**, 664–668 (2013).

79. Zhan ZB, Lei Y. Sub-100-nm nanoparticle arrays with perfect ordering and tunable and uniform dimensions fabricated by combining nanoimprinting with ultrathin alumina membrane technique. *ACS Nano* **8**, 3862–3868 (2014).
80. Xiang JX, Wang YX, Wu YP et al. Superplastic nanomolding of highly ordered metallic sub-micrometer pillars arrays for surface enhanced Raman scattering. *Adv Mater Technol* **7**, 2100891 (2022).
81. Jeon NJ, Noh JH, Kim YC et al. Solvent engineering for high-performance inorganic-organic hybrid perovskite solar cells. *Nat Mater* **13**, 897–903 (2014).
82. Permyakov DV, Kondratiev VI, Pidgayko DA et al. Probing optical losses and dispersion of fully guided waves through critical evanescent coupling. *JETP Lett* **113**, 780–786 (2021).
83. McPeak KM, Jayanti SV, Kress SJP et al. Plasmonic films can easily be better: rules and recipes. *ACS Photonics* **2**, 326–333 (2015).
84. Boidin R, Halenkovič T, Nazabal V et al. Pulsed laser deposited alumina thin films. *Ceram Int* **42**, 1177–1182 (2016).

Acknowledgements

The work was supported by the Federal Program 'Priority 2030' and NSFC (Project 62350610272). A. K. Samusev acknowledges Deutsche Forschungsgemeinschaft – project No.529710370. The authors are thankful to Nina Sheremet, Volodymyr Sheremet, Hüseyin Bilge Yağcı, and Hamed Dehghanpour Baruj for assistance with the experiments at Bilkent University UNAM, and Mikhail Baranov for assistance with the experiments at ITMO University. The authors thank Mr. Ivan Pustovit for assistance in graphic design.

Author contributions

M. A. Masharin provided the thin film fabrication, conducted the optical experiments, developed the concept, and analyzed experimental data. D. Khmelevskaia synthesized perovskite nanocuboids and nanoplates, provided experiments with nanocuboids, characterized the plasmonic substrate, and analyzed the experimental and theoretic results. V. I. Kondratiev provided the experimental setup for SIL angle-resolved spectroscopy measurement and helped with experiments with it. D. I. Markina provided the synthesis of the perovskite nanowhiskers and participated in the optical experiments. A. D. Utyushev provided the theoretical model for multimode analysis of perovskite nanocuboids and simulated the scattering radiation pattern. A. D. Dmitriev provided the theoretical estimation of the $CsPbBr_3$ refractive index at 6 K. V. A. Shahnazaryan provided the theoretical model of stimulated polariton relaxation. A. P. Pushkarev supervised the fabrication process. F. Isik participated in the SEM measurements and plasmonic substrates fabrication. I. V. Iorsh and I. A. Shelykh supervised the theoretical part of the work. H. V. Demir supervised the experimental part of the work. A.K.M. suggested the main concept of the polariton-assisted stimulated emission and supervised the experimental work. S. V. Makarov managed the whole project. All authors extensively discussed the results and participated in editing the manuscript.

Competing interests

The authors declare no competing financial interests.

Supplementary information

Supplementary information for this paper is available at https://doi.org/10.29026/oea.2024.230148

Scan for Article PDF